ACCSCIENCE PUBLISHING

International Journal of Bioprinting

RESEARCH ARTICLE

A novel bilayer cell-free 3D-printed scaffold for osteochondral defect repair

Beini Mao[1,2,3,4,5]*, Jintao Zhong[1,2], Yu-Ching Hsu[1], Zerun Mao[5], Xindi Wan[5], Yujian Jiang[1,2], Hetong Li[1,3]*, and Hongxun Sang[1,2]*

[1]Department of Orthopedic Surgery, Shenzhen Hospital, Southern Medical University, Shenzhen, Guangdong, China

[2]Department of Surgery, Shenzhen School of Clinical Medicine, Southern Medical University, Shenzhen, Guangdong, China

[3]International Sports Medicine and Rehabilitation Center, Shenzhen Hospital, Southern Medical University, Shenzhen, Guangdong, China

[4]Department of Rehabilitation Medicine, Shenzhen Hospital, Southern Medical University, Shenzhen, Guangdong, China

[5]Department of Physical Therapy, School of Rehabilitation Sciences, Southern Medical University, Guangzhou, Guangdong, China

***Corresponding authors:**
Beini Mao (maobeini187@163.com);
Hetong Li (heatonlee@outlook.com);
Hongxun Sang (hxsang@smu.edu.cn)

Citation: Mao B, Zhong J, Hsu Y-C, *et al*. A novel bilayer cell-free 3D-printed scaffold for osteochondral defect repair. *Int J Bioprint*. doi: 10.36922/IJB026420452

Received: October 14, 2026

Revised: October 27, 2026

Accepted: November 11, 2026

Published online: November 20, 2026

Copyright: © 2026 Author(s). This is an Open-Access article distributed under the terms of the Creative Commons Attribution License, permitting distribution, and reproduction in any medium, provided the original work is properly cited.

Publisher's Note: AccScience Publishing remains neutral with regard to jurisdictional claims in published maps and institutional affiliations.

Abstract

Articular cartilage defects are difficult to repair due to inferior regenerative capacity and complex structural integration between cartilage and subchondral bone. Conventional clinical treatments often cause fibrocartilage formation and unsatisfactory long-term outcomes. To address these limitations, we developed a bilayer, cell-free osteochondral scaffold fabricated by low-temperature extrusion-based 3D printing using gelatin methacryloyl (GelMA). The cartilage layer was functionalized with dopamine-modified hyaluronic acid (DHA) to enhance bone marrow mesenchymal stem cell (BMSC) migration and chondrogenic differentiation in vitro. The subchondral bone layer incorporated nano-hydroxyapatite (nHAp) to provide osteoinductive cues and mechanical support for bone regeneration. The physicochemical properties, printability, mechanical performance, and biocompatibility of the scaffolds were systematically characterized. In vitro studies demonstrated that the GelMA/DHA layer significantly enhanced BMSCs migration and upregulated chondrogenic markers, while the GelMA/nHAp layer promoted osteogenic differentiation. In a rabbit osteochondral defect model, the bilayer scaffold facilitated coordinated regeneration of hyaline-like cartilage and subchondral bone, as evidenced by gross evaluation, micro-computed tomography analysis, and histological staining. This spatially organized, cell-free strategy combines complementary cartilage- and bone-supportive cues and promotes coordinated osteochondral repair. The proposed bilayer scaffold offers a promising biomaterial-based approach for osteochondral defect repair without exogenous cell transplantation.

Keywords: Osteochondral defect; Gelatin methacryloyl; Dopamine; Hyaluronic acid; Nano-hydroxyapatite; Cartilage regeneration; Three-dimensional printing

1. Introduction

Articular cartilage is a specialized avascular and alymphatic connective tissue that plays an essential role in load bearing, shock absorption, and joint lubrication. Owing to its limited intrinsic regenerative capacity, cartilage defects rarely heal spontaneously and often progress to osteoarthritis.[1] The prevalence of cartilage disorders is increasing with population aging and the rising incidence of sports-related injuries.[2-4] Clinical investigations have reported that cartilage lesions are detected in up to 60% of patients undergoing arthroscopy, and severe defects frequently lead to chronic pain, joint dysfunction, and eventual degenerative joint disease.[3,5]

Current therapeutic options for cartilage defects include microfracture, osteochondral autograft transplantation, autologous chondrocyte implantation, and joint replacement. Although these approaches may provide temporary symptomatic relief, they are often associated with fibrocartilage formation, donor site morbidity, limited graft availability, and unsatisfactory long-term outcomes.[6-8] Therefore, strategies capable of restoring durable hyaline cartilage and reconstructing the osteochondral unit remain urgently needed.

Tissue engineering has emerged as a promising alternative for cartilage repair. Various natural polymers, such as gelatin, collagen, hyaluronic acid (HA), and chitosan, as well as synthetic polymers including poly(lactic-co-glycolic acid), polycaprolactone, and polyethylene glycol, have been explored as scaffold materials.[9-11] Among them, hydrogel-based systems have attracted particular attention due to their favorable biocompatibility, tunable mechanical properties, and biomimetic extracellular matrix-like microenvironment.[12] For instance, previous studies have demonstrated that gelatin methacryloyl (GelMA) hydrogels support chondrocyte viability and matrix deposition, while the incorporation of HA further enhances chondrogenic phenotype maintenance and extracellular matrix production, highlighting the potential of GelMA/HA composite systems in cartilage regeneration.[13] Recent studies in other tissue-repair settings have further demonstrated that functionalized polysaccharide hydrogels and hierarchical polymer composites can integrate controlled therapeutic delivery, environmental responsiveness, and multiscale structural support to promote tissue regeneration.[14-16] However, despite significant advances, several translational limitations remain. Cell-based scaffold strategies generally require cell sourcing, ex vivo expansion, and quality-controlled manufacturing, which increase the time, cost, and logistical complexity of treatment.[17] The survival of transplanted mesenchymal stem cells (MSCs) may also be compromised after implantation by the hypoxic and nutrient-poor environment within tissue-engineered constructs.[18] Furthermore, articular cartilage and subchondral bone differ markedly in their structural, mechanical, and biological requirements; thus, repair of the osteochondral unit requires coordinated consideration of both compartments.[19,20] Homogeneous or single-phase constructs may be insufficient to reproduce these region-specific microenvironments, which has motivated the development of layered, multiphasic, and gradient scaffolds capable of presenting spatially organized cues.[19,20]

To overcome these challenges, we developed a bilayer, cell-free osteochondral scaffold fabricated via low-temperature extrusion-based three-dimensional (3D) printing. GelMA was employed as a printable matrix because of its photo-crosslinkable properties and cytocompatibility. The cartilage layer was functionalized with dopamine-modified HA (DHA) to provide cartilage-supportive cues and to evaluate its effects on bone marrow mesenchymal stem cells (BMSCs) migration and chondrogenic differentiation in vitro. The subchondral bone layer incorporated nano-hydroxyapatite (nHAp) to provide osteoinductive and mechanical support for bone regeneration. This spatially organized design was intended to support coordinated cartilage and subchondral bone repair without exogenous cell transplantation.

2. Materials and methods

2.1. Preparation of GelMA/DHA and GelMA/nHAp precursor formulations

Dopamine-modified HA was synthesized using HA via an 1-ethyl-3-(3-dimethylaminopropyl) carbodiimide/N-hydroxysuccinimide-mediated amide coupling reaction, with reference to previous work.[21] Briefly, high-molecular weight HA (400 mg, 1 mmol) was dissolved in 200 mL of ultra-pure water under continuous stirring at room temperature until a clear solution was obtained. Subsequently, 1-ethyl-3-(3-dimethylaminopropyl) carbodiimide (960 mg, 5 mmol) and N-hydroxysuccinimide (230 mg, 2 mmol) were introduced to activate the carboxyl groups of HA at pH 4.75–5.0 for 2 h. The reaction mixture was then purged with nitrogen for 30 min to reduce oxidative interference. Dopamine hydrochloride (569 mg, 3 mmol), dissolved in 10 mL ultra-pure water, was added dropwise under constant pH regulation, and the reaction was allowed to proceed for 24 h. The final product was purified by dialysis against ultra-pure water for 72 h, followed by freezing and lyophilization to obtain DHA powder.

To fabricate GelMA/DHA hydrogels, 10% (w/v) GelMA, 2.4% (w/v) DHA, and 0.5% (w/v) lithium phenyl-2,4,6-trimethylbenzoylphosphinate (LAP) were dissolved

in phosphate-buffered saline (PBS) at 55 °C under continuous stirring for 1 h to ensure complete dissolution and homogeneous mixing. All reactions were conducted under light-protected conditions.

The GelMA/nHAp hydrogel precursor was prepared by incorporating nHAp into a GelMA matrix with ultrasonic-assisted dispersion. Briefly, nHAp powder was first suspended in PBS and ultrasonicated for 20–30 min to ensure uniform particle dispersion and minimize aggregation. The pre-dispersed nHAp suspension was then mixed with GelMA and LAP to achieve final concentrations of 10% (w/v) GelMA, 2% (w/v) nHAp, and 0.5% (w/v) LAP.

The mixture was maintained at 55 °C under continuous magnetic stirring for 1 h to facilitate complete dissolution of GelMA and homogeneous distribution of nHAp particles throughout the hydrogel precursor.

2.2. Sample preparation

After preparation, the GelMA, GelMA/DHA, and GelMA/nHAp precursor formulations were used to fabricate specimens for physicochemical characterization and in vivo implantation. For physicochemical characterization, each formulation was cast into cylindrical molds measuring 4 mm in diameter and 4 mm in height. The molded specimens were photocrosslinked using an external handheld 405-nm light source for at least 5 s.

Scaffolds intended for implantation were fabricated using an extrusion-based 3D bioprinter (BIO X, CELLINK AB, Sweden) equipped with a 25-gauge nozzle. All three formulations were printed using similar nominal conditions. The cartridge and printbed temperatures were maintained at 25 °C and 4 °C, respectively. The nominal printing speed was 2 mm/s, the layer height was 0.25 mm, and the extrusion pressure was adjusted within 60–100 kPa according to the extrusion behavior of each formulation. Minor real-time adjustments to the pressure and printing speed were made when necessary to maintain continuous filament deposition and geometric fidelity.

All implantable scaffolds had an overall diameter of 4 mm and a height of 4 mm. In the bilayer scaffold, the 1-mm-thick cartilage layer was printed as a solid layer, whereas the 3-mm-thick subchondral bone layer consisted of concentric rings interconnected by a cross-shaped framework. The cartilage layer was always printed first, followed by the subchondral bone layer, to avoid collapse during fabrication. All implantable scaffolds were fabricated under aseptic conditions within a biosafety cabinet. The built-in photocuring module of the printer was not used. After the entire construct had been printed, including both layers of the bilayer scaffold, it was photocrosslinked using the external 405-nm handheld light source for at least 5 s. To eliminate the influence of the structure, the GelMA, GelMA/DHA, and GelMA/nHAp single-material scaffolds were printed with the same overall dimensions and geometry as the bilayer scaffold, but each scaffold was fabricated entirely using the corresponding single hydrogel formulation. General images of the samples used for physicochemical characterization and animal experiments are provided in the Appendix.

2.3. Characterization of each layer of the scaffold

Fourier transform infrared (FTIR) spectroscopy was used to analyze the chemical structures and functional groups of GelMA, GelMA/DHA, and GelMA/nHAp. Lyophilized samples were finely ground into powders and examined using an FTIR spectrometer. Spectra were collected in the range of 4,000–400 cm^{-1} with a resolution of 4 cm^{-1}. All spectra were baseline-corrected and normalized to facilitate comparison of characteristic absorption bands.

X-ray diffraction (XRD) analysis was conducted to evaluate the crystalline structure and phase composition of GelMA, GelMA/DHA, and GelMA/nHAp hydrogels. Freeze-dried samples were analyzed using an X-ray diffractometer with Cu Kα radiation operated at 40 kV and 40 mA. Diffraction patterns were recorded over a 2θ range of 10°–80° with a step size of 0.02° and a scanning rate of 2°/min. The obtained diffraction profiles were compared with standard reference patterns to confirm the presence of crystalline structure.

Temperature-dependent rheological measurements were conducted using a rotational rheometer equipped with a 25-mm parallel plate. An appropriate amount of precursor solution was loaded onto the stage maintained at 50 °C, with a fixed gap of 1 mm. Small-amplitude oscillatory shear tests were performed at 1 Hz and 1% strain, within the linear viscoelastic range. A cooling ramp from 40 °C to 10 °C at 5s/°C was applied, and storage modulus (G') and loss modulus (G") between 15 °C and 35 °C were continuously recorded. The sol–gel transition temperature was determined at the G'/G" crossover point.

The molded cylindrical specimens described above were used for uniaxial compression testing. Samples were compressed at a constant displacement rate of 0.1 mm/s on a universal testing machine until damage was detected by the machine or 90% strain was reached. Stress–strain curves were continuously recorded, and the elastic modulus was calculated manually. At least three samples per group were tested, and results were reported as mean ± standard deviation.

The rheological properties of the photocrosslinked cylindrical hydrogels during the heating process were also evaluated. Temperature sweep measurements were

performed over a range of 15–60 °C at a constant oscillation frequency (1 Hz) and a fixed strain within the linear viscoelastic region (typically 1%). The storage modulus (G') and loss modulus (G") were continuously recorded as functions of temperature, as reported above.

The internal morphology of the molded GelMA, GelMA/DHA, and GelMA/nHAp specimens was examined using scanning electron microscopy (SEM; IMAGING 100, Raycision Medical Technology Co., Ltd., China). Hydrogels prepared in deionized water were fixed in 2.5% glutaraldehyde overnight at 4 °C and rinsed three times with deionized water. Samples were then freeze-dried, quenched in liquid nitrogen, and fractured at the center to expose the cross-section. The fractured surfaces were sputter-coated with gold and observed under SEM. Pore size and porosity were quantified from SEM images using ImageJ software (version 1.46r, National Institutes of Health, USA). Three independently prepared specimens were analyzed per group ($n = 3$), using the exposed central cross-section. Images were calibrated using the scale bar and converted to 8-bit grayscale. Pores were segmented by manually adjusting the threshold to distinguish dark pore regions from the scaffold walls, and the segmentation masks were verified against the original images. Individual pores were automatically detected using "Analyze Particles"; boundary-truncated pores and obvious artifacts were excluded. Pore size was defined as the equivalent circular diameter, $D = 2\sqrt{(A/\pi)}$, calculated from the segmented pore area (A). Pore diameters were averaged within each specimen. SEM-derived area porosity was calculated as the total segmented pore area divided by the analyzed cross-sectional area.

Enzymatic degradation was evaluated using collagenase P (0.01 mmol/L) at 37 °C. The molded GelMA, GelMA/DHA, and GelMA/nHAp specimens described above were freeze-dried and weighed to obtain the initial dry weight (W_0). Separate independently prepared specimens were assigned to each measurement time point and were not returned to the degradation medium after measurement. The specimens were immersed in collagenase solution and incubated at 37 °C under gentle shaking. Every 24 h, samples were collected, rinsed with deionized water, freeze-dried, and weighed to determine the remaining dry weight (W_t). The degradation ratio was calculated as $W_t/W_0 \times 100\%$. If the hydrogel fragmented during degradation, all remaining pieces were collected from the centrifuge tube prior to lyophilization and weighing. Three independent specimens were analyzed per group at each time point ($n = 3$). The experiment was terminated when the samples were completely degraded and could no longer be collected.

The swelling behavior of the hydrogels was evaluated using a gravimetric method. Hydrogels prepared in PBS were immersed in deionized water at room temperature. Every 30 min, samples were removed, gently blotted with filter paper to remove excess surface water, and weighed immediately. The swelling ratio was calculated as the ratio of the wet weight at each time point to the initial weight of the hydrogel. Measurements were continued until the hydrogel weight reached equilibrium.

2.4. Biological properties of the scaffolds

Rat BMSCs were isolated from femurs and tibias of Sprague–Dawley rats ($n = 4$) for the following experiment. After euthanasia, the bones were aseptically harvested and surrounding soft tissues were removed. Both ends of the bones were cut, and the bone marrow cavity was flushed with culture medium using a syringe. The collected cell suspension was gently pipetted to obtain a homogeneous mixture and centrifuged to remove the supernatant. The cell pellet was resuspended in complete low-glucose Dulbecco's Modified Eagle Medium (DMEM) supplemented with 10% fetal bovine serum and cultured at 37 °C in a humidified atmosphere with 5% CO_2. After 24 h, non-adherent cells were removed by medium replacement. The medium was subsequently changed every 2–3 days.

The cytocompatibility of the scaffolds was evaluated using a Cell Counting Kit-8 (CCK-8) assay (Cat. No. GOY-0369E, Guangzhou Huayun Biotechnology Co., Ltd., China). Extracts of GelMA, GelMA/DHA, and GelMA/nHAp hydrogels were prepared by incubating the samples in low-glucose DMEM at 37 °C for 24 h. Low-glucose DMEM served as the blank control. Passage 3 (P3) BMSCs were seeded into 96-well plates at a density of 5×10^5 cells/mL and cultured overnight. The medium was then replaced with the corresponding hydrogel extracts supplemented with 5% fetal bovine serum. Cell viability was assessed from day 1 to day 7 using CCK-8 working solution according to the manufacturer's instructions. Absorbance was measured at 450 nm using a microplate reader in four independent samples per group at each time point ($n = 4$).

To evaluate the effects of different scaffold layers on BMSCs differentiation, gene expression of osteogenic and chondrogenic markers was analyzed by quantitative real-time polymerase chain reaction (PCR). BMSCs were seeded onto GelMA, GelMA/DHA, and GelMA/nHAp hydrogels and cultured for the designated period. Total RNA was extracted using a commercial RNA extraction kit according to the manufacturer's instructions. Briefly, cell-laden hydrogels were mechanically disrupted, lysed, and centrifuged to obtain the supernatant. RNA was purified using spin columns, washed, and eluted in RNase-

free water. The concentration and purity of RNA were determined prior to reverse transcription. Complementary DNA (cDNA) was synthesized using a reverse transcription kit, followed by quantitative PCR amplification using specific primers. Chondrogenic-related genes (*Col2a1* and *Sox9*) and osteogenic-related genes (*Col1a1* and *Runx2*) were selected for analysis. GAPDH was used as the internal reference gene. Relative gene expression levels were calculated using the $2^{-\Delta\Delta Ct}$ method and normalized to the control group.

A Transwell migration assay was performed to evaluate the effects of different hydrogels on BMSC migration. BMSCs were seeded into the upper chamber of Transwell inserts, while GelMA, GelMA/DHA, and GelMA/nHAp hydrogels were placed in the lower chambers and fully immersed in culture medium. After 48 h of incubation, cells that had migrated to the lower surface were fixed and stained with crystal violet. Migrated cells were observed under a light microscope and quantified by cell counting. The migration-promoting effects of the hydrogels were evaluated by comparing the number of migrated cells among the groups.

2.5. *In vivo* osteochondral defect repair in rabbits

The *in vivo* repair performance of the scaffolds was evaluated using a rabbit knee osteochondral defect model. Male New Zealand rabbits weighing 1.8–2.2 kg were obtained from the Guangdong Medical Laboratory Animal Center ($n = 20$; Sanshui Base, China). All rabbit procedures were approved by the Institutional Animal Care and Use Committee of Shenzhen Lingfu Topu Biotechnology Co., Ltd. (Approval No. TOPGM-IACUC-2023-0154; approved on November 20, 2023) and were conducted in accordance with the institutional guidelines for the care and use of laboratory animals. Animals were randomly divided into five groups: control (untreated), GelMA, GelMA/DHA, GelMA/nHAp, and bilayer scaffold, resulting in two rabbits and four knee specimens per group at each time point. Both knees of each rabbit received the same intervention, and the animals allocated to the 6- and 12-week endpoints were independent cohorts. Rabbits were weighed and anesthetized before surgery. The hair around the anterior region of both knees was shaved, followed by routine disinfection and sterile draping. A longitudinal skin incision was made along the medial side of the patella. The fascia and muscle layers were bluntly dissected, and the joint capsule was incised longitudinally along the medial patellar border. With the knee extended, the patella was dislocated laterally, and the joint cavity was exposed by flexing the knee to visualize the femoral condyles. Under knee flexion, a cylindrical osteochondral defect (4 mm in diameter and 4 mm in depth) was created at a site located between the femoral condyles, approximately 3 mm above the intercondylar fossa, using a trephine bur. The defect surface was flattened with a curette to ensure uniform geometry. In the experimental groups, the printed scaffolds prepared as described above were implanted into the defect site, while defects in the control group were left unfilled. The joint capsule and skin were sutured layer by layer. Postoperatively, penicillin (400,000 units per rabbit) was administered intramuscularly once daily for three consecutive days to prevent infection. Animals were housed individually and allowed free activity.

At 6 and 12 weeks postoperatively, the rabbits were sacrificed, and both distal femurs were harvested. The defect sites were photographed for gross evaluation. Macroscopic repair was assessed using the International Cartilage Repair Society (ICRS) macroscopic scoring system for its reliability and history of application in rabbit focal osteochondral defect models.[22,23]

To evaluate subchondral bone regeneration, harvested distal femur samples were scanned using a micro-computed tomography (micro-CT) system. A cylindrical region of interest (ROI) corresponding to the original defect area was selected for quantitative analysis. The same threshold value was applied to all samples to distinguish mineralized tissue from non-mineralized tissue. Bone volume fraction (BV/TV), trabecular thickness (Tb.Th), trabecular separation (Tb.Sp), trabecular number (Tb.N), and trabecular pattern factor (Tb.Pf) were calculated to assess subchondral bone repair.

For histological analysis, harvested femoral samples were fixed in 4% paraformaldehyde, decalcified, dehydrated, embedded in paraffin, and sectioned into 4 μm-thick slices. Sections were stained with hematoxylin and eosin, Masson's trichrome, and Safranin O–Fast Green according to standard protocols to evaluate tissue morphology, collagen deposition, and cartilage matrix formation. For immunohistochemical analysis, sections were deparaffinized, subjected to antigen retrieval, and incubated with primary antibodies against collagen type 1 (COL1), collagen type 2 (COL2), and aggrecan, followed by appropriate secondary antibodies. Signals were visualized using a 3,3'-diaminobenzidine substrate system and counterstained with hematoxylin. Cartilage repair quality was semi-quantitatively evaluated using the Safranin O–Fast Green staining subscore (0–6) of the rabbit-specific Osteoarthritis Research Society International (OARSI) histopathology recommendations, together with the Mankin scoring system.[24,25] The positive staining area of immunohistochemical markers was quantified using ImageJ software.

The surgical procedures, specimen collection, and

outcome assessments were performed by different investigators, and the assessors were blinded. No animals or samples were excluded from the analysis.

2.6. Statistical analysis

Quantitative data are presented as mean ± standard deviation. The CCK-8 assay used four independent samples per group at each time point ($n = 4$), whereas quantitative real-time qPCR and Transwell used three ($n = 3$). Technical replicate wells or multiple microscopic fields were averaged to obtain one value for each independent sample before statistical analysis. Single-time-point comparisons were performed using one-way analysis of variance, whereas data involving both group and time were analyzed using two-way analysis of variance, including the group × time interaction. Pairwise comparisons between groups within each time point were adjusted using the Holm procedure. For bilateral animal outcomes, measurements from both knees of each rabbit were averaged to obtain one animal-level value before inferential analysis; therefore, the statistical sample size was two rabbits per group at each time point, although four knee-level observations are displayed in the figures. ICRS, OARSI, and Mankin scores were analyzed as continuous variables. No animals or samples were excluded from the analysis. All tests were two-sided, and $p < 0.05$ was considered statistically significant. Exact p-values are reported to three decimal places, whereas values below 0.001 are reported as $p < 0.001$. Statistical analyses were performed using R, and graphs were generated using GraphPad Prism (8, GraphPad Software, Inc., USA).

3. Results

3.1. Chemical structure of materials

The synthesis of GelMA, GelMA/DHA, and GelMA/nHAp was confirmed using FTIR (Figure 1A). GelMA exhibited characteristic absorption peaks at approximately 1,646 cm^{-1} (amide I) and 1,524 cm^{-1} (amide II), corresponding to the gelatin backbone. This characteristic was retained in GelMA/DHA and GelMA/nHAp, indicating that the polymer backbone remained structurally intact following composite formation. The amide bond formed between HA and dopamine enhanced the amide I absorption peak at 1,640 cm^{-1}, and its slight shift suggests the formation of secondary interactions, likely hydrogen bonding, between GelMA and DHA. For the GelMA/nHAp composite, new peaks appeared at around 604 cm^{-1} and 560 cm^{-1}, which are characteristic of the phosphate (PO_4^{3-}) vibrations of hydroxyapatite (HAp), confirming the successful incorporation of nHAp into the hydrogel matrix. In general, all syntheses were successful, and the modification method was moderate.

X-ray diffraction analysis was performed to examine the crystalline phase of hydrogels (Figure 1B). GelMA and GelMA/DHA exhibited a broad diffuse halo, indicative of their predominantly amorphous polymeric structure. In contrast, GelMA/nHAp displayed some distinct diffraction peaks, corresponding to the characteristic crystal planes of nHAp, confirming the successful incorporation of nHAp into the GelMA matrix without altering its crystalline structure.

3.2. Rheological properties of the precursor solution

Temperature-dependent rheological analysis was conducted to evaluate the sol–gel transition behavior of GelMA, GelMA/DHA, and GelMA/nHAp precursor solutions during cooling (Figure 1C). For all three hydrogel precursors, the storage modulus (G') gradually surpassed the loss modulus (G") during cooling. The G'–G" crossover temperature was approximately 25 °C for GelMA, 21 °C for GelMA/DHA, and 22 °C for GelMA/nHAp.

3.3. Compressive mechanical properties of the hydrogels

The uniaxial compression test results showed that although the incorporation of DHA and nHAp did not significantly alter the elastic modulus of GelMA (both $p > 0.05$), the GelMA/nHAp hydrogel designed for the subchondral bone layer exhibited a significantly higher compressive modulus than the GelMA/DHA hydrogel used for the cartilage layer ($p = 0.049$). In addition, GelMA/nHAp (16.20 MPa) demonstrated a trend toward a higher modulus compared with GelMA (13.53 MPa) (Figure 1D).

3.4. Rheological properties of crosslinked hydrogels

The rheological behavior of the hydrogel changed after photocrosslinking. During heating, all photocrosslinked hydrogels exhibited a gradual decrease in storage modulus (G'), while G' remained consistently higher than the loss modulus (G"), indicating stable elastic-dominant behavior (Figure 2A).

3.5. Internal structure of the scaffold

Scanning electron microscopy images revealed that all three photocrosslinked hydrogels exhibited a highly porous and interconnected internal microstructure (Figure 2B). Pore size analysis showed that both GelMA/DHA and GelMA/nHAp exhibited significantly larger average pore sizes than GelMA (both $p < 0.001$), while no significant difference was detected between GelMA/DHA and GelMA/nHAp (Figure 2C). Porosity analysis showed that GelMA possessed the highest overall porosity, with a significant reduction ($p = 0.017$) observed in the GelMA/nHAp group (Figure 2D).

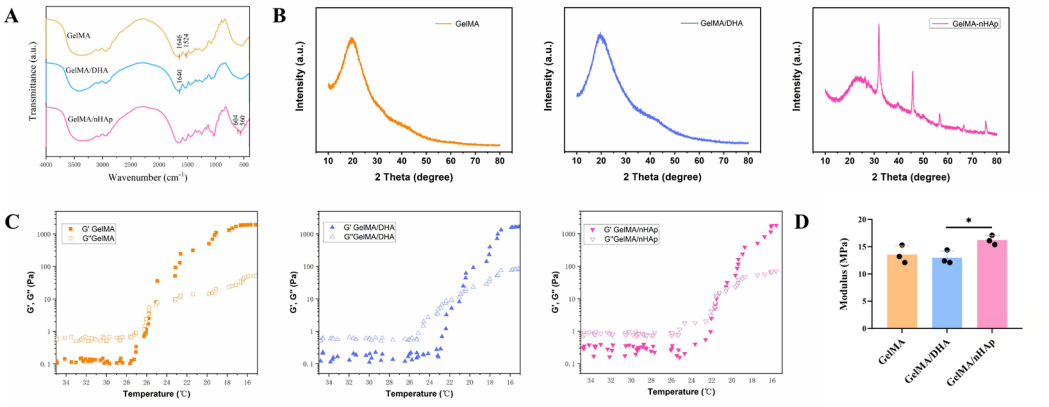


Figure 1. Physicochemical and mechanical characterization of GelMA-based hydrogels. (A) Fourier transform infrared spectra of GelMA, GelMA/DHA, and GelMA/nHAp hydrogels. The characteristic amide I and amide II peaks of GelMA are observed around 1,646 and 1,524 cm^{-1}. GelMA/DHA shows enhanced absorption near 1,640 cm^{-1}, while GelMA/nHAp exhibits additional phosphate-related peaks at approximately 604 and 560 cm^{-1}, confirming successful incorporation of DHA and nHAp, respectively. (B) X-ray diffraction patterns of GelMA, GelMA/DHA, and GelMA/nHAp hydrogels. GelMA and GelMA/DHA display broad diffraction peaks characteristic of amorphous structures, whereas GelMA/nHAp presents distinct crystalline diffraction peaks corresponding to hydroxyapatite, indicating the successful introduction of nHAp into the hydrogel matrix. (C) Temperature-dependent rheological analysis of GelMA, GelMA/DHA, and GelMA/nHAp precursor solutions. Storage modulus (G') and loss modulus (G") were measured during temperature variation, demonstrating thermosensitive gelation behavior and suitable viscoelastic properties for extrusion-based three-dimensional printing. (D) Compressive modulus of different hydrogels. GelMA/nHAp exhibits a significantly higher compressive modulus compared with GelMA/DHA.
Notes: Error bars represent the standard deviation; $^*p < 0.05$.
Abbreviations: DHA: Dopamine-modified hyaluronic acid; GelMA: Gelatin methacryloyl; nHAp: Nano-hydroxyapatite.

3.6. Degradation behavior of the hydrogels

All groups exhibited progressive degradation under enzymatic conditions (Figure 2E). At day 4, GelMA/DHA showed significantly greater loss than GelMA (p = 0.042). GelMA/DHA and GelMA/nHAp had completely disintegrated by day 5, whereas GelMA remained measurable until day 6.

3.7. Swelling behavior of the hydrogels

All hydrogel groups exhibited time-dependent swelling ratios (Figure 2F). At 30 min, the swelling ratio of GelMA/DHA was significantly higher than those of GelMA (p < 0.001) and GelMA/nHAp (p = 0.006). No significant group differences were detected at 60 min. At 90 min, GelMA/DHA remained significantly higher than GelMA (p = 0.002) and GelMA/nHAp (p = 0.007). The corresponding differences remained significant at 120 min (p = 0.008 and 0.031, respectively).

3.8. Cytocompatibility of hydrogels

The cytocompatibility of GelMA, GelMA/DHA, and GelMA/nHAp hydrogels to BMSCs was evaluated using a CCK-8 assay (Figure 3A). Cell metabolic activity increased progressively over time in both control and extract-treated groups. Across all time points, no significant cytotoxic effects were observed in any extract group compared to the control group, indicating good biosafety of all hydrogel formulations. Notably, cells cultured in GelMA/DHA extract exhibited significantly higher viability compared with the control group at later time points (p = 0.016 and 0.030 on day 6 and 7, respectively).

3.9. Material-induced lineage-specific differentiation of BMSCs

The expression levels of *Col2a1* in the GelMA/DHA group were significantly higher than those in the GelMA (p = 0.003) and GelMA/nHAp groups (p = 0.006). *Sox9* expression was also significantly higher in GelMA/DHA than in both GelMA and GelMA/nHAp (both p = 0.002, Figure 3B). In contrast, *Col1a1* expression in the GelMA/nHAp group was significantly higher than that in the GelMA (p = 0.001) and GelMA/DHA groups (p = 0.004). *Runx2* expression was likewise significantly higher in GelMA/nHAp than in the other two groups (both p < 0.001, Figure 3C).

3.10. Evaluation of bone marrow mesenchymal stem cell migration

The Transwell migration assay was used to evaluate the effects of the different hydrogels on BMSC migration. Representative images showed markedly more migrated BMSCs in the GelMA/DHA group than in the GelMA and GelMA/nHAp groups (Figure 3D). Quantitative

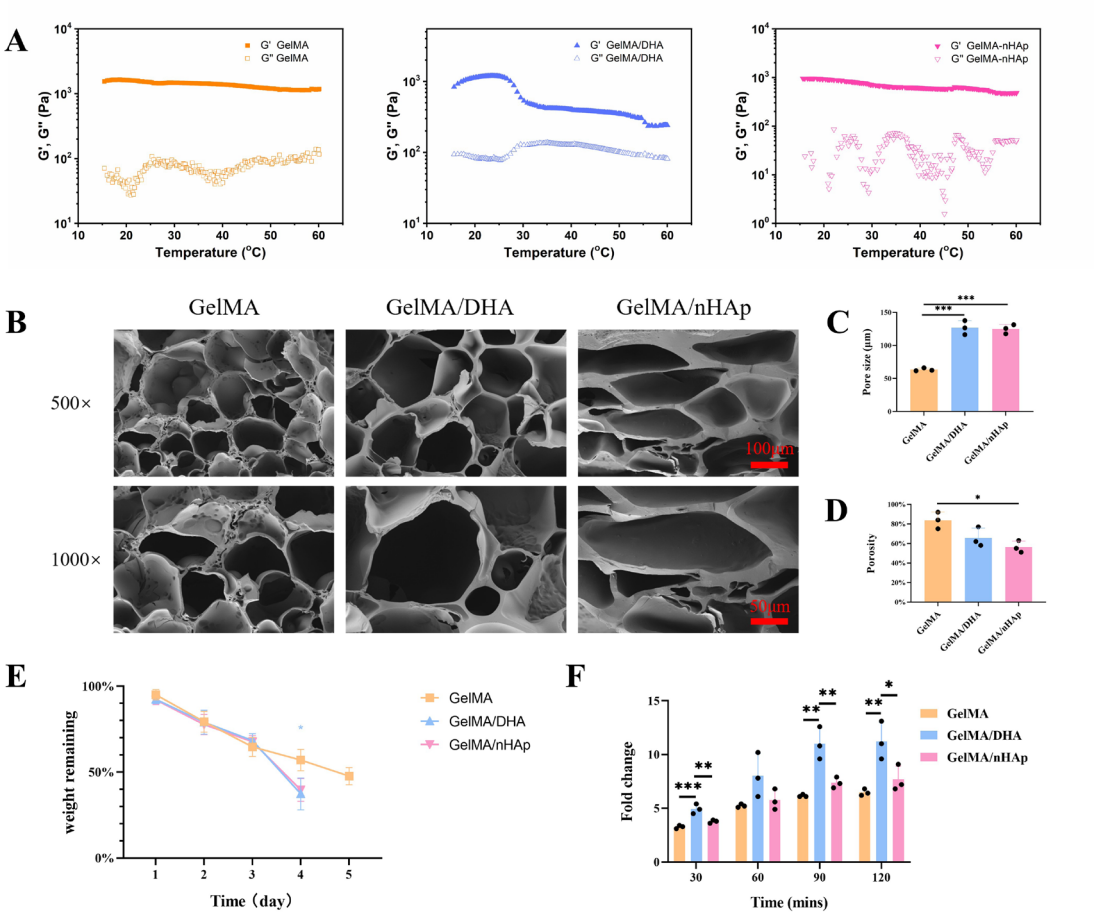


Figure 2. Microstructural characteristics and physicochemical properties of GelMA-based hydrogels. (A) Temperature sweep rheological analysis of GelMA, GelMA/DHA, and GelMA/nHAp hydrogels. Storage modulus (G′) and loss modulus (G″) were measured from 15 to 60 °C. All groups exhibited stable viscoelastic behavior, with G′ consistently higher than G″, indicating formation of a stable crosslinked network suitable for structural maintenance. (B) Representative scanning electron microscopy images of the internal porous structures. Scale bars: 100 μm, 50 μm; magnifications: 500×, 1,000×. All hydrogels displayed interconnected porous structures. GelMA/DHA and GelMA/nHAp showed enlarged pore architecture compared with pure GelMA. (C) Quantitative analysis of pore size distribution. The average pore size of GelMA/DHA and GelMA/nHAp hydrogels was significantly larger than that of GelMA. (D) Porosity measurement of different hydrogel groups. GelMA exhibited the highest porosity, while incorporation of DHA and nHAp slightly reduced overall porosity. (E) Enzymatic degradation expressed as the percentage of dry weight remaining. All hydrogels showed time-dependent degradation, with GelMA/DHA and GelMA/nHAp demonstrating relatively accelerated mass loss compared with GelMA (blue * GelMA /DHA vs. GelMA, $p < 0.05$). (F) Swelling ratio of the hydrogels. GelMA/DHA exhibited the highest swelling capacity among the groups, indicating enhanced hydrophilicity after DHA incorporation.

Notes: Error bars represent the standard deviation among samples; *$p < 0.05$; **$p < 0.01$; and ***$p < 0.001$.

Abbreviations: DHA: Dopamine-modified hyaluronic acid; GelMA: Gelatin methacryloyl; nHAp: Nano-hydroxyapatite.

analysis confirmed that the number of migrated cells was significantly higher in the GelMA/DHA group than in the GelMA ($p = 0.003$) and GelMA/nHAp groups ($p = 0.003$). No significant difference was observed between the GelMA and GelMA/nHAp groups (Figure 3E).

3.11. Macroscopic view of repaired cartilage

Macroscopic observation revealed clear differences in cartilage defect repair among groups at both 6 and 12 weeks (Figure 4A). At 6 weeks, the control group showed poor defect filling. The GelMA group exhibited limited repair, while the GelMA/DHA and GelMA/nHAp groups demonstrated improved defect coverage and smoother surfaces. Notably, the bilayer scaffold group presented the most complete defect filling and the best surface continuity, resembling native cartilage morphology.

At 12 weeks, repair outcomes further improved across all treatment groups. The bilayer group continued to show

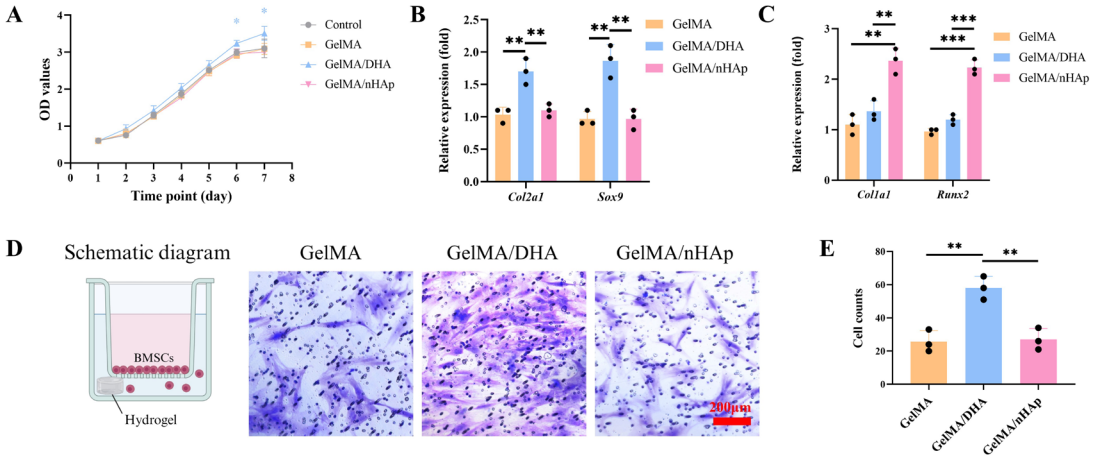


Figure 3. Biological properties of GelMA-based hydrogels. (A) Cytocompatibility assessed by Cell Counting Kit-8 assay. OD values increased progressively in all groups, indicating good cytocompatibility. GelMA/DHA showed significantly enhanced cell proliferation at later time points (blue * GelMA/DHA vs. Control, $p < 0.05$). (B) Relative mRNA expression levels of chondrogenic markers in BMSCs cultured with different hydrogels. GelMA/DHA significantly upregulated *Col2a1* and *Sox9* expression compared with GelMA and GelMA/nHAp, indicating enhanced chondrogenic differentiation potential. (C) Relative mRNA expression levels of osteogenic markers. GelMA/nHAp markedly increased *Col1a1* and *Runx2* expression compared with other groups, demonstrating its osteoinductive capability. (D) Schematic illustration of the Transwell migration assay and representative crystal violet–stained images of migrated BMSCs. Scale bar: 200 μm; magnification: 100×. (E) Quantification of migrated cells. GelMA/DHA significantly increased BMSCs migration compared with GelMA and GelMA/nHAp.

Notes: Error bars represent the standard deviation among samples; *$p < 0.05$; **$p < 0.01$; ***$p < 0.001$.

Abbreviations: BMSCs: Bone marrow mesenchymal stem cells; DHA: Dopamine-modified hyaluronic acid; GelMA: Gelatin methacryloyl; nHAp: Nano-hydroxyapatite; OD: Optical density.

the most homogeneous cartilage-like tissue and superior integration with surrounding native cartilage, whereas the GelMA/DHA and GelMA/nHAp groups also maintained favorable repair quality, outperforming the GelMA and control groups.

Quantitative evaluation using the ICRS cartilage repair scoring system supported the gross observations (Figure 4B). At 6 weeks, the mean scores were 0.75, 2.75, 8.75, 6.25, and 10.75 in the control, GelMA, GelMA/DHA, GelMA/nHAp, and bilayer groups, respectively. The GelMA/DHA group had significantly higher scores than the control and GelMA groups (both $p < 0.001$), while the GelMA/nHAp group scored significantly higher than the control ($p = 0.002$) and GelMA groups ($p = 0.024$). The bilayer group scored significantly higher than the control and GelMA groups (both $p < 0.001$) and the GelMA/nHAp group ($p = 0.006$), but did not differ significantly from the GelMA/DHA group ($p = 0.150$). At 12 weeks, the mean scores were 4.50, 6.50, 11.50, 10.50, and 12.00 in the respective groups. The GelMA/DHA group scored significantly higher than the control ($p < 0.001$) and GelMA groups ($p = 0.003$). Similarly, the GelMA/nHAp group scored significantly higher than the control ($p = 0.001$) and GelMA groups ($p = 0.013$), while the bilayer group scored significantly higher than the control ($p < 0.001$) and GelMA groups ($p = 0.002$). No significant differences were detected between the GelMA/DHA and GelMA/nHAp groups ($p = 0.688$), between the GelMA/DHA and bilayer groups ($p = 0.688$), or between the GelMA/nHAp and bilayer groups ($p = 0.501$). Mean scores were descriptively higher at 12 weeks than at 6 weeks in all groups.

3.12. Evaluation of subchondral bone

Representative micro-CT images showed progressive filling of the subchondral defect from 6 to 12 weeks, with comparatively more mineralized tissue visible in the GelMA/nHAp and bilayer groups (Figure 5A). However, quantitative analysis revealed no significant within-time-point differences in BV/TV or Tb.Th among the five groups at either 6 or 12 weeks (Figure 5B and 5C). At 6 weeks, Tb.Sp was significantly lower in the GelMA/nHAp and bilayer groups than in the GelMA group ($p = 0.026$ and 0.039, respectively; Figure 5D). At 12 weeks, Tb.N was significantly higher in the GelMA/nHAp and bilayer groups than in the GelMA/DHA group ($p = 0.024$ and 0.028, respectively; Figure 5E). Tb.Pf was significantly lower in the bilayer group than in the GelMA/DHA group at 6 weeks ($p = 0.044$), whereas no significant group differences were detected at 12 weeks (Figure 5F). No other within-time-point pairwise comparisons reached

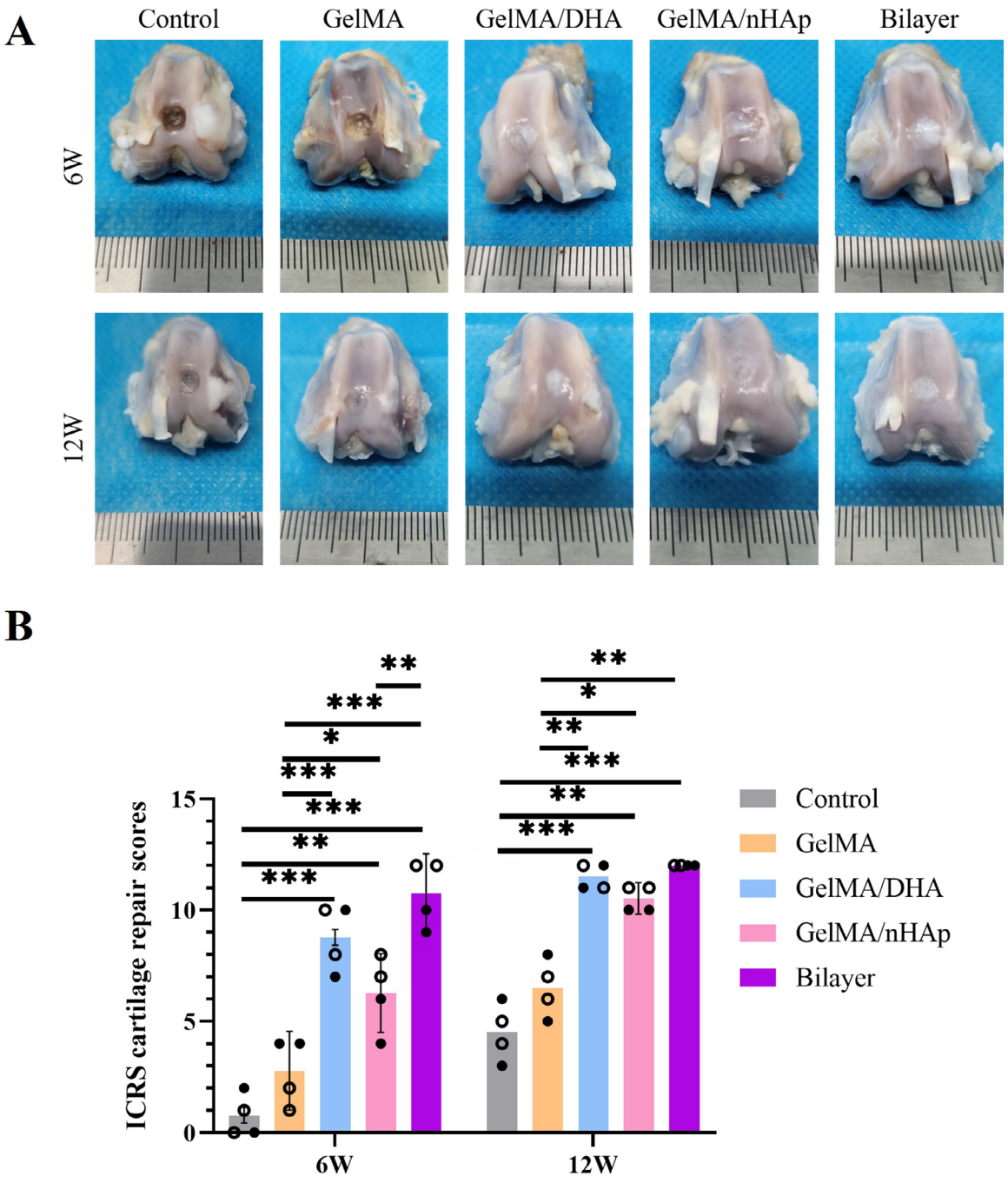


Figure 4. Gross observation and macroscopic evaluation of osteochondral defect repair *in vivo*. (A) Representative macroscopic images of osteochondral defects at 6 and 12 weeks after implantation. At 6 weeks, the bilayer group exhibited more complete defect filling and smoother surface morphology compared with other scaffolds. At 12 weeks, the bilayer scaffold showed more continuous integration with surrounding tissue and restoration of cartilage-like appearance. (B) ICRS macroscopic cartilage repair scores at 6 and 12 weeks. Higher scores indicate better macroscopic repair. Four knee-joint scores are displayed for each group at each time point. The two knees obtained from the same rabbit are indicated using the same symbol style (open or filled circles).

Notes: Error bars represent the corresponding animal-level standard deviation; $^{*}p < 0.05$; $^{**}p < 0.01$; $^{***}p < 0.001$.

Abbreviations: DHA: Dopamine-modified hyaluronic acid; GelMA: Gelatin methacryloyl; ICRS: International Cartilage Repair Society; nHAp: Nano-hydroxyapatite.

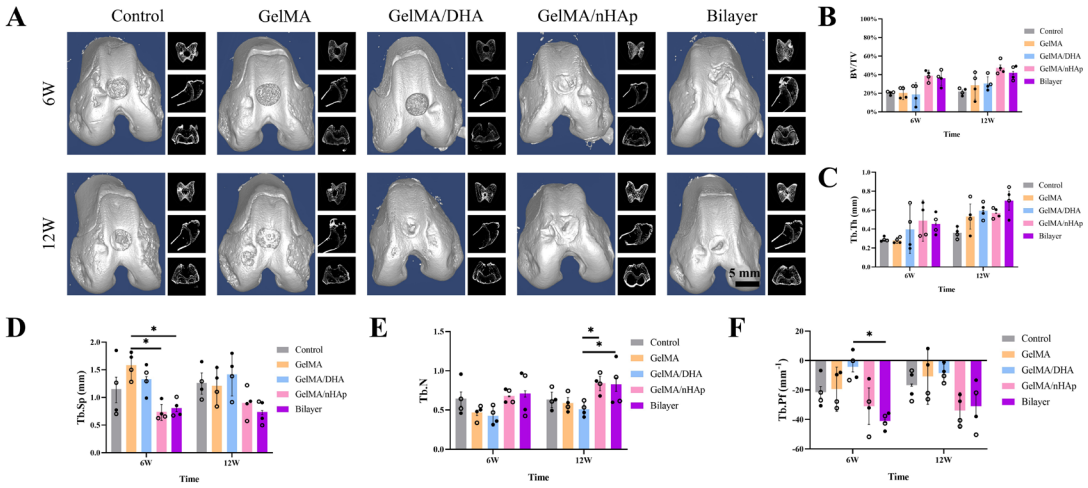


Figure 5. Micro-CT evaluation of subchondral bone regeneration *in vivo*. (A) Representative three-dimensional reconstructed micro-CT images and corresponding cross-sectional views of osteochondral defects at 6 and 12 weeks after implantation. The bilayer and GelMA/nHAp scaffolds exhibited more substantial bone defect filling and improved structural integrity compared with some other groups, particularly at 12 weeks. (B–F) Quantitative micro-CT analysis of subchondral bone parameters, including (B) bone volume fraction (BV/TV), (C) trabecular thickness (Tb.Th), (D) trabecular separation (Tb.Sp), (E) trabecular number (Tb.N), and (F) trabecular pattern factor (Tb.Pf). Four knee-joint values are displayed for each group at each time point. The two knees obtained from the same rabbit are indicated using the same symbol style (open or filled circles).
Notes: Error bars represent the corresponding animal-level standard deviation; *$p < 0.05$; **$p < 0.01$; ***$p < 0.001$.
Abbreviations: DHA: Dopamine-modified hyaluronic acid; GelMA: Gelatin methacryloyl; Micro-CT: Micro-computed tomography; nHAp: Nano-hydroxyapatite.

statistical significance.

3.13. Histological evaluation

Histological staining revealed distinct repair patterns among the groups (Figure 6A–C). At 12 weeks, the GelMA/DHA and bilayer groups exhibited smoother and more continuous cartilage-like tissue, although subchondral bone formation remained incomplete in the GelMA/DHA group. Masson's trichrome staining showed bone-like tissue extending into the cartilage region in the GelMA/nHAp group at 6 weeks. Safranin O–Fast Green staining demonstrated stronger cartilage matrix staining in the GelMA/DHA and bilayer groups, whereas the GelMA/nHAp group exhibited relatively weak cartilage staining at 6 weeks.

At 6 weeks, the OARSI scores of the GelMA/DHA, GelMA/nHAp, and bilayer groups were lower than those of the control group (all $p < 0.001$) and the GelMA group ($p = 0.008$, $p < 0.001$, and $p < 0.001$, respectively). The bilayer group also had lower scores than the GelMA/DHA and GelMA/nHAp groups ($p = 0.002$ and 0.041, respectively). At 12 weeks, these three groups had lower scores than the control group (all $p < 0.001$) and the GelMA group ($p = 0.004$, 0.009, and $p < 0.001$, respectively), with no significant differences among them (Figure 6D).

Mankin scoring showed a similar pattern (Figure 6E). At 6 weeks, the GelMA/DHA, GelMA/nHAp, and bilayer groups had lower scores than the control group ($p = 0.003$, 0.006, and $p < 0.001$, respectively) and the GelMA group ($p = 0.024$, 0.045, and $p < 0.001$, respectively), with no significant differences among these three groups. At 12 weeks, all treatment groups had lower scores than the control group ($p = 0.036$, $p < 0.001$, $p = 0.002$, and $p < 0.001$ for GelMA, GelMA/DHA, GelMA/nHAp, and bilayer, respectively). The GelMA/DHA and bilayer groups also had lower scores than the GelMA group ($p = 0.005$ and $p < 0.001$), and the bilayer group had a lower score than the GelMA/nHAp group ($p = 0.009$).

3.14. Immunohistochemical staining

Immunohistochemical staining showed stronger COL1 expression in the GelMA and GelMA/nHAp groups, whereas COL2 and AGG staining were more intense and continuous in the GelMA/DHA and bilayer groups (Figure 7A–C).

At 6 weeks, the COL1-positive areas in the GelMA and GelMA/nHAp groups were greater than those in the control, GelMA/DHA, and bilayer groups (all $p < 0.001$). At 12 weeks, the GelMA group showed greater COL1-positive areas than the control, GelMA/DHA, and bilayer groups ($p = 0.028$, 0.003, and 0.006, respectively), while the

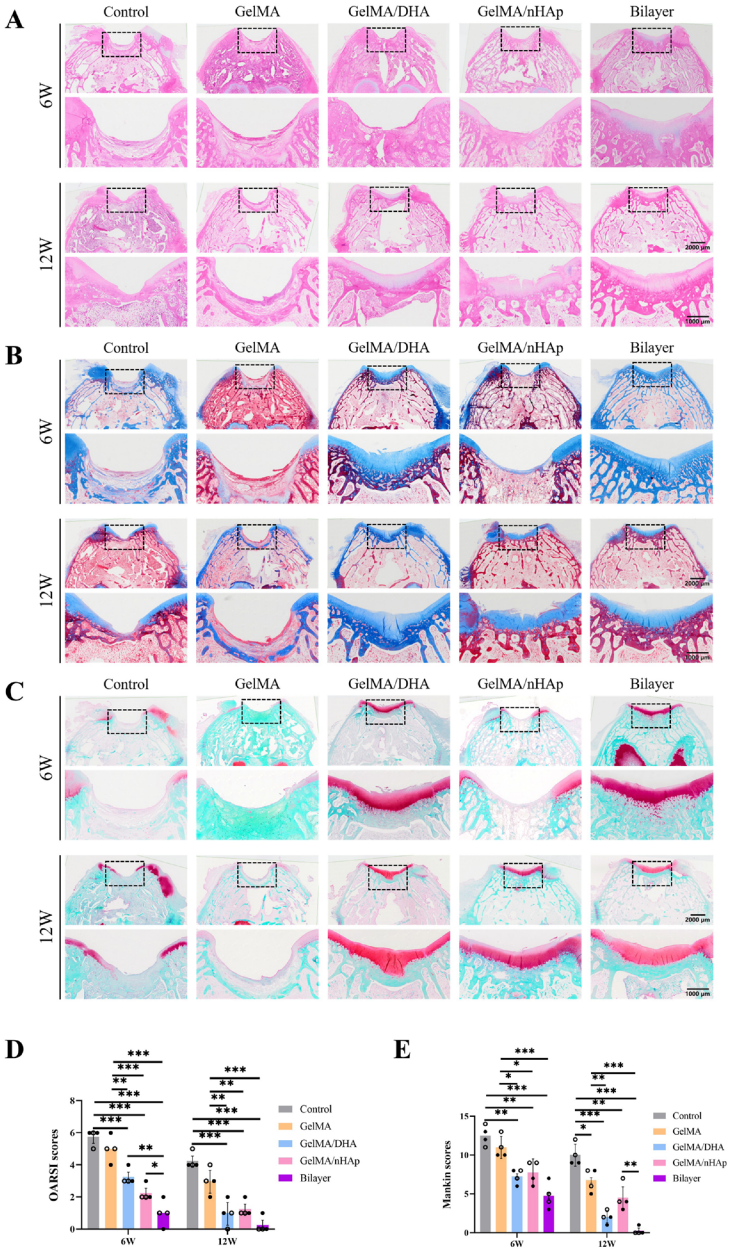


Figure 6. Histological evaluation of cartilage regeneration *in vivo*. (A) Representative hematoxylin and eosin staining images. The cartilage morphology in the control group was incomplete, whereas subchondral bone was absent in the GelMA and GelMA/DHA groups. Scale bars: 2,000 μm, 1,000 μm. (B) Representative Masson staining images. At 6 weeks, the GelMA/nHAp group showed weak staining in cartilage. At 12 weeks, the GelMA/DHA group exhibited faint staining in the subchondral bone region. In contrast, the control and GelMA groups showed little to no repair. Scale bars: 2,000 μm, 1,000 μm. (C) Representative images of Safranin O–Fast Green staining. It showed enhanced cartilage filling and stronger matrix deposition in the GelMA/DHA and bilayer groups, with matrix in the GelMA/DHA group extending into the defect region. In contrast, the GelMA/nHAp group exhibited weak cartilage staining at 6 weeks, indicating limited cartilage regeneration. Scale bars: 2,000 μm, 1,000 μm. (D) Quantitative OARSI scores. The bilayer group showed significantly lower scores compared with some other groups at 6 and 12 weeks (*$p < 0.05$). (E) Mankin scores of regenerated cartilage. The bilayer scaffold generally showed lower scores, indicating superior cartilage repair quality. Dashed boxes in the low-magnification images indicate the regions shown at higher magnification. Lower OARSI and Mankin scores indicate better histological repair. Four knee-joint scores are displayed for each group at each time point. The two knees obtained from the same rabbit are indicated using the same symbol style (open or filled circles).
Notes: Error bars represent the corresponding animal-level standard deviation; *$p < 0.05$; **$p < 0.01$; ***$p < 0.001$.
Abbreviations: DHA: Dopamine-modified hyaluronic acid; GelMA: Gelatin methacryloyl; nHAp: Nano-hydroxyapatite; OARSI: Osteoarthritis Research Society International.

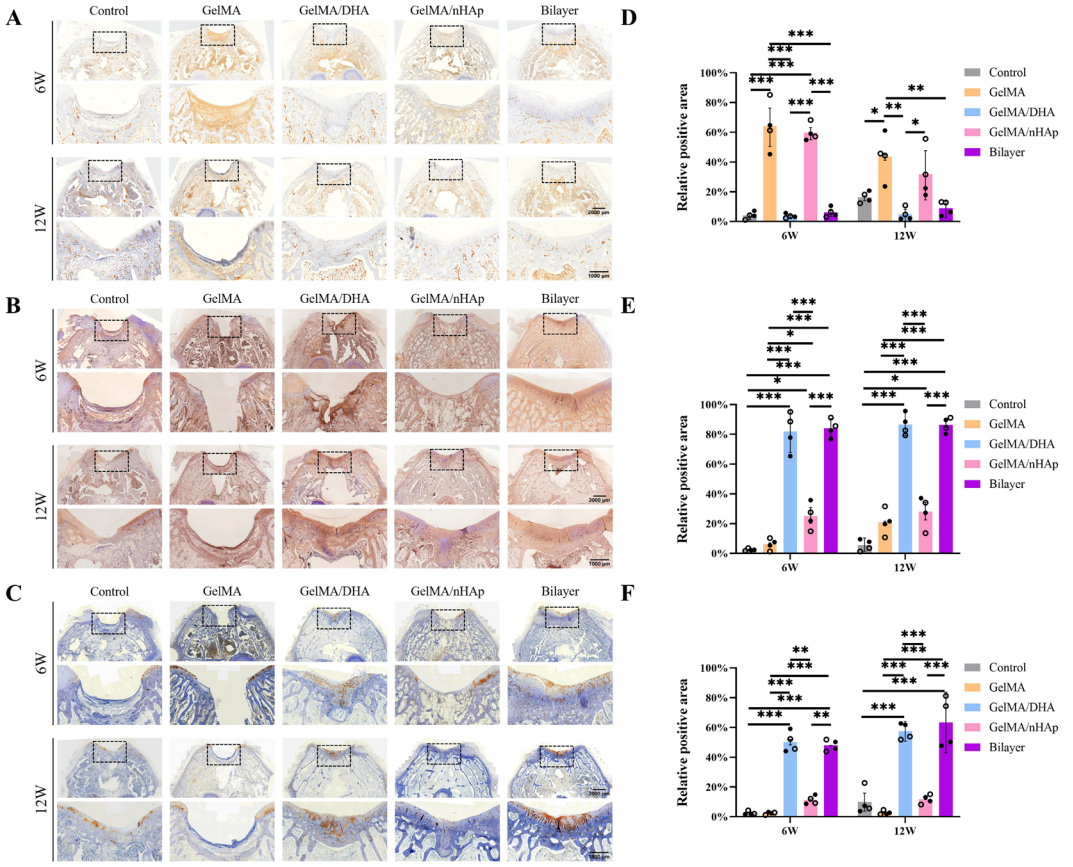


Figure 7. Immunohistochemical evaluation of regenerated tissue. Representative immunohistochemical staining for (A) COL1, (B) COL2, and (C) AGG at 6 and 12 weeks after implantation. Scale bars: 2,000 μm, 1,000 μm. (D–F) Quantification of relative positive area for (D) COL1, (E) COL2, and (F) AGG. Dashed boxes in the low-magnification images indicate the regions shown at higher magnification. Four knee-joint values are displayed for each group at each time point. The two knees obtained from the same rabbit are indicated using the same symbol style (open or filled circles). Error bars represent the corresponding animal-level standard deviation. $^{*}p < 0.05$, $^{**}p < 0.01$, and $^{***}p < 0.001$.
Abbreviations: AGG: Aggrecan; COL1: Collagen type 1; COL2: Collagen type 2; DHA: Dopamine-modified hyaluronic acid; GelMA: Gelatin methacryloyl; nHAp: Nano-hydroxyapatite.

GelMA/nHAp group showed a greater positive area than the GelMA/DHA group ($p = 0.028$, Figure 7D).

At both time points, the COL2-positive areas in the GelMA/DHA and bilayer groups were greater than those in the control, GelMA, and GelMA/nHAp groups (all $p < 0.001$). The GelMA/nHAp group also showed greater COL2-positive areas than the control and GelMA groups at 6 weeks ($p = 0.019$ and 0.039) and the control group at 12 weeks ($p = 0.020$, Figure 7E).

The AGG-positive areas in the GelMA/DHA and bilayer groups were greater than those in the control and GelMA groups at 6 weeks (all $p < 0.001$) and greater than those in the GelMA/nHAp group (both $p = 0.002$). At 12 weeks, the GelMA/DHA and bilayer groups showed greater AGG-positive areas than all other groups (all $p < 0.001$, Figure 7F).

4. Discussion

The present study developed a spatially organized, cell-free osteochondral scaffold containing a DHA-functionalized cartilage layer and an nHAp-containing subchondral bone layer.GelMA/DHA enhanced BMSC migration and chondrogenic marker expression in vitro, whereas GelMA/nHAp increased osteogenic marker expression. In the rabbit osteochondral defect model, the bilayer scaffold produced a comparatively balanced combination of cartilage- and subchondral bone-related repair outcomes. The principal contribution of this study is therefore the integration of complementary cartilage- and bone-supportive material environments within a single 3D-printed construct. However, the *in vivo* findings do not directly demonstrate recruitment of endogenous BMSCs. FTIR and XRD analyses supported the successful incorporation of DHA and nHAp

into the GelMA-based formulations. FTIR spectra verified that the incorporation of bioactive components did not disrupt the fundamental polymer network and supported the successful establishment of secondary intermolecular interactions that may contribute to matrix mimicry. This mild synthesis method means that the new material will inherit some of the properties of GelMA, which is the basis for some functions of the scaffolds. XRD results demonstrated that GelMA and GelMA/DHA maintained an amorphous structure, consistent with the viscoelastic nature of soft cartilage-like matrices, whereas GelMA/nHAp exhibited characteristic diffraction peaks associated with HAp, which retained the crystalline characteristics of HAp and contributed to the relative mechanical differences between the layer-specific formulations.[26] This was also confirmed by the results of subsequent uniaxial compression experiments. GelMA/nHAp also exhibited a higher compressive modulus than GelMA/DHA, although neither modified formulation differed significantly from GelMA. The precursor formulations retained thermoresponsive behavior, with G'/G" crossover temperatures of approximately 21 °C–25 °C, providing a practical processing window for low-temperature extrusion. Following photocrosslinking, G' remained higher than G" over the measured temperature range, indicating elastic-dominant behavior of the crosslinked hydrogels. SEM confirmed that the hydrogel has a porous, interconnected structure, while the modified hydrogel has larger pores and lower porosity. This indicates that the modified hydrogels have a denser network structure and larger channels, which may benefit cell adhesion and migration. GelMA/DHA and GelMA/nHAp also underwent relatively rapid enzymatic degradation in vitro, thus could disappear after the cartilage and subchondral bone regenerate. GelMA/DHA exhibited the greatest swelling capacity, consistent with the hydrophilic characteristics of the DHA-containing network.[27] Collectively, these results demonstrate that incorporation of DHA and nHAp modified the physical properties of GelMA while preserving its suitability for hydrogel scaffold fabrication.

These findings are consistent with the broader development of multifunctional polymeric biomaterials that combine structural support with application-specific biological functions. For example, sodium hyaluronate-based hydrogels have been designed to integrate sustained short interfering RNA delivery, tissue adhesion, and microenvironmental protection, whereas glucose-responsive chitosan-based composite nanohydrogels have combined responsive release with antibacterial, anti-inflammatory, and pro-angiogenic activities.[15,16] Hierarchical chitosan/polyvinyl alcohol/polyethylene glycol composite membranes have similarly demonstrated how micro- and nanoscale organization can regulate water absorption, permeability, dimensional stability, and cytocompatibility.[14] In the present study, this general design principle was applied by spatially separating DHA-containing and nHAp-containing formulations to provide distinct material environments for cartilage and subchondral bone repair.

The CCK-8 results showed that none of the hydrogel extracts reduced BMSC metabolic activity relative to the control, supporting the cytocompatibility of the formulations. GelMA/DHA produced higher metabolic activity at the later time points. This effect may be attributed to DHA, which potentially endows the hydrogel with improved bioactivity and enhanced cell adhesion and growth-promoting properties. Previous studies have reported that dopamine-functionalized materials can strengthen cell–matrix interactions, thereby improving cell viability and proliferative capacity.[28]

Regarding lineage-specific differentiation, GelMA/DHA promoted the expression of chondrogenic markers, whereas GelMA/nHAp preferentially enhanced the expression of osteogenic markers. DHA is highly hydrophilic, and HA is a major component of the native cartilage extracellular matrix. Our findings are consistent with a previous report showing that a DHA-containing hydrogel supported BMSC chondrogenic differentiation.[21] HA has also been reported to potentiate transforming growth factor-β3-induced chondrogenesis through SOX9/ERK/Smad-associated signaling in another MSC model.[29] However, because these signaling events were not examined in the present study, the molecular mechanism underlying the effects of GelMA/DHA remains to be established. In contrast, nHAp, as the principal inorganic component of bone tissue, provides osteoinductive cues that can stimulate BMSCs' osteogenic differentiation through activation of *Runx2*, *Col1a1*, and other osteogenesis-related genes, ultimately promoting bone formation.[30]

The Transwell assay demonstrated that GelMA/DHA enhanced BMSC migration in vitro. This finding suggests that the DHA-containing hydrogel may provide a microenvironment favorable for cell migration. However, the Transwell assay does not demonstrate that endogenous bone marrow-derived BMSCs migrated into the implanted scaffold in vivo. Although the anatomical proximity of the osteochondral defect to the subchondral bone marrow provides a plausible route for host-cell migration, this proposed mechanism requires direct verification using in vivo cell tracking or lineage-tracing approaches.

The macroscopic, histological, and immunohistochemical findings supported the cartilage-related effects of the DHA-containing layer. At 6 weeks,

the bilayer group achieved a higher ICRS score than the GelMA/nHAp group and lower OARSI scores than both single-composition functionalized groups, although its ICRS score did not differ significantly from that of GelMA/DHA. At 12 weeks, the differences among the GelMA/DHA, GelMA/nHAp, and bilayer groups were less pronounced for several scoring outcomes. Nevertheless, the GelMA/DHA and bilayer groups consistently exhibited comparatively strong COL2 and aggrecan staining, supporting the formation of a more cartilage-like extracellular matrix. In comparison, the GelMA/nHAp group showed relatively greater COL1 staining and less COL2 and aggrecan staining than the GelMA/DHA and bilayer groups. Because hyaline cartilage is characterized by abundant type 2 collagen and aggrecan, whereas COL1-rich fibrocartilaginous repair tissue has less favorable long-term mechanical properties, these results support the inclusion of the DHA-containing cartilage layer.[10,31-33]

The micro-CT results suggested comparatively greater mineralized tissue formation in the GelMA/nHAp and bilayer groups. Quantitative analysis, however, showed no significant differences in BV/TV or Tb.Th among the groups at either time point. GelMA/nHAp and the bilayer scaffold exhibited lower Tb.Sp than GelMA at 6 weeks and higher Tb.N than GelMA/DHA at 12 weeks, while the bilayer group also showed a lower Tb.Pf than GelMA/DHA at 6 weeks. These results suggest that the nHAp-containing scaffolds influenced selected aspects of trabecular organization rather than producing consistent improvement in all micro-CT parameters. Importantly, because the animal-level sample size was limited to two rabbits per group at each time point, the absence of statistically significant differences in some parameters may partly reflect insufficient statistical power and should not be interpreted as evidence that the groups were equivalent. Together with the bone-associated histological findings, these results suggest that the GelMA/nHAp formulation supported a degree of subchondral bone repair.

Overall, the *in vitro* findings support the migration-promoting and chondrogenic effects of GelMA/DHA and the osteogenic effect of GelMA/nHAp. The *in vivo* findings suggest that combining these components within a bilayer scaffold produced a more balanced osteochondral repair profile than the individual formulations, although the bilayer scaffold was not significantly superior to both single-composition scaffolds for every outcome.

A recent study has used a system similar to GelMA/DHA for bone repair and showed that the system could induce osteogenic differentiation of BMSCs, with photothermal stimulation further enhancing this effect.[34] In contrast, our GelMA/DHA scaffold preferentially promoted chondrogenic differentiation rather than osteogenesis. This difference may be related to differences in crosslinking strategy and mechanical microenvironment. In their study, Fe^{3+}-mediated dual crosslinking significantly reinforced the hydrogel network, resulting in elevated mechanical stiffness that is known to bias mesenchymal stem cell fate toward osteogenic lineage commitment. Indeed, accumulating evidence indicates that matrix stiffness and mechanical cues play a decisive role in directing stem cell differentiation, with stiffer substrates favoring osteogenesis and softer matrices supporting chondrogenesis.[35] In contrast, we deliberately adopted a milder hydrogen bond-based interaction between DHA and GelMA, preserving a softer, more hydrated, cartilage-like microenvironment. This design better recapitulates the native extracellular matrix of articular cartilage and provides mechanical and biochemical cues conducive to chondrogenic differentiation.[36]

Another previous study reached similar results to our study, showing that DHA-integrated COL1 hydrogel can promote chondrogenic differentiation.[21] Compared with them, we further confirmed its regenerative efficacy in a rabbit model in addition to in vitro validation, strengthening the translational relevance of this approach. Moreover, by using GelMA, our system enables low-temperature extrusion printing and rapid photo-crosslinking, allowing precise scaffold fabrication while preserving bioactivity, which represents a practical advantage over previously reported platforms. Furthermore, our scaffold design explicitly acknowledges the critical role of subchondral bone in osteochondral repair, rather than focusing solely on cartilage regeneration. Subchondral bone is essential for providing mechanical support, metabolic exchange, and biochemical signaling that collectively influence cartilage homeostasis and repair outcomes.[37] To address this, we integrated a nHAp–reinforced subchondral bone layer, leveraging the well-established osteoconductive and osteoinductive properties of nHAp.[38] Notably, the two layers were sequentially deposited within the same 3D-printing workflow, enabling spatial organization of two formulations within a single construct. The *in vivo* findings support the feasibility of this design strategy. The importance of scaffold architecture at the osteochondral interface is also supported by a recent computational and experimental study showing that extrusion-printed interface designs can modulate stress distribution and interfacial mechanical performance.[39]

A previous study developed a gelatin-based osteochondral organoid system containing HA and HAp, in which BMSCs were precultured and induced toward lineage-specific differentiation before implantation.[40] In

contrast, our scaffold was implanted without exogenous cell seeding or predifferentiation, thereby avoiding the need for in vitro cell expansion. Recent work has similarly highlighted the translational potential of acellular 3D-printed cartilage scaffolds, showing that biochemical functionalization with cartilage extracellular matrix and an MSC-affinity peptide can enhance cartilage repair without exogenous cell loading.[41] The enhanced BMSC migration observed in vitro suggests that the DHA-containing layer may favor host-cell ingress after implantation. However, this remains a proposed mechanism because endogenous BMSC migration was not directly tracked in vivo. Furthermore, while their system utilized conventional HAp, we incorporated nHAp, which enhances bioactivity. There has been evidence suggesting that nHAp possesses superior osteoinductive properties compared with conventional HAp, due to its higher surface area, enhanced protein adsorption, and improved mechanical cues that collectively promote BMSCs' osteogenic differentiation.[42] The *in vivo* results confirmed that the repair strategy adopted in our study achieved satisfactory outcomes as early as three months, which is earlier than the 6-month time point reported in the aforementioned study.

Beyond the above advantages, our system also presents additional strengths compared with previous studies. We deliberately employed high-molecular-weight HA, rather than low-molecular-weight HA commonly used in prior studies. Our previous work has demonstrated that high-molecular-weight HA can enhance hyaline cartilage regeneration by promoting macrophage M2 polarization and reinforcing chondrogenic differentiation.[43] Its incorporation into the GelMA/DHA layer may therefore provide additional biological benefits. However, macrophage polarization and other immune responses were not evaluated in the present study, and an immunomodulatory mechanism cannot be concluded from the current results.

Several limitations of this study should be acknowledged. First, the animal-level sample size was limited to two rabbits per group at each time point. This limited statistical power, particularly for the micro-CT outcomes, and the animal results should therefore be interpreted cautiously and confirmed in larger cohorts. Second, the same overall geometry was used for all implantable scaffolds to minimize the influence of scaffold architecture when comparing the effects of different material compositions. The concentric-ring and cross-shaped printed structure was strategically designed to provide interconnected pathways that may facilitate cell migration and tissue ingrowth. However, the independent contribution of this architecture to osteochondral repair was not evaluated in the present study. Third, although GelMA/DHA enhanced BMSC migration in vitro, endogenous BMSCs were not directly tracked after implantation. Endogenous BMSC recruitment should therefore be regarded as a proposed mechanism rather than a demonstrated in vivo process. Future studies using cell labeling, lineage tracing, or specific stem-cell markers are required to determine the origin and fate of the cells participating in tissue repair. Finally, the animal model employed represents an acute osteochondral defect, whereas most clinical cartilage lesions in humans are chronic and degenerative in nature. Therefore, the therapeutic efficacy of this strategy in chronic models remains to be validated.

5. Conclusion

In this study, we developed a 3D-printed bilayer osteochondral scaffold integrating DHA and nHAp to provide region-specific regenerative cues. The DHA-containing cartilage layer enhanced BMSC migration and chondrogenic marker expression in vitro, whereas the nHAp-containing bone layer promoted osteogenic marker expression. In vivo, the bilayer scaffold supported coordinated restoration of cartilage and subchondral bone. These findings demonstrate the potential of spatially organized, cell-free biomaterials for osteochondral repair, while the possible contribution of endogenous BMSC recruitment requires direct in vivo verification.

Acknowledgments

None.

Funding

The work was funded by Guangdong Basic and Applied Basic Research Foundation (2023A1515110336), the 2026 Undergraduate Innovation and Entrepreneurship Training Program of Southern Medical University (S202612121164; 202612121334), Guangdong Provincial Engineering Technology Research Center for Clinical Translation and Application of Medical 3D Printing Materials (2023B192), and Guangdong-HongKong-Macao Joint Innovation Field (2025A0505080015). The funders had no role in any part of the study or decision on publication.

Conflict of interest

The authors declare no competing interests.

Author contributions

Conceptualization: Beini Mao, Hongxun Sang
Data curation: Beini Mao, Jintao Zhong, Hetong Li
Formal analysis: Beini Mao, Yu-Ching Hsu
Funding acquisition: Beini Mao, Zerun Mao, Xindi Wan,

Hongxun Sang
Project administration: Zerun Mao, Xindi Wan
Software: Yujian Jiang
Supervision: Hongxun Sang
Writing–original draft: Beini Mao
Writing–review & editing: Beini Mao

Ethics approval and consent to participate

Animal studies in this work were approved by Shenzhen Lingfu Topu Biotechnology Co., Ltd. Laboratory Animal Management and Use Committee (TOPGM-IACUC-2023-0154).

Consent for publication

Not applicable.

Availability of data

All data are available upon reasonable request from the corresponding authors.

AI tools statement

Generative large language models (ChatGPT; GPT-5, OpenAI, USA) were used in order to improve the language. The authors reviewed and edited the content as needed and take full responsibility for the content of the published article.

References

1. Sophia Fox AJ, Bedi A, Rodeo SA. The basic science of articular cartilage: structure, composition, and function. *Sports Health*. 2009;1(6):461-468.

   doi: 10.1177/1941738109350438

2. Arøen A, Løken S, Heir S, *et al*. Articular cartilage lesions in 993 consecutive knee arthroscopies. *Am J Sports Med*. 2004;32(1):211-215.

   doi: 10.1177/0363546503259345

3. Widuchowski W, Widuchowski J, Trzaska T. Articular cartilage defects: study of 25,124 knee arthroscopies. *Knee*. 2007;14(3):177-182.

   doi: 10.1016/j.knee.2007.02.001

4. Zhang Y, Jordan JM. Epidemiology of osteoarthritis. *Clin Geriatr Med*. 2010;26(3):355-369.

   doi: 10.1016/j.cger.2010.03.001

5. Hunter DJ, Bierma-Zeinstra S. Osteoarthritis. *Lancet*. 2019;393(10182):1745-1759.

   doi: 10.1016/S0140-6736(19)30417-9

6. Kreuz PC, Steinwachs MR, Erggelet C, *et al*. Results after microfracture of full-thickness chondral defects in different compartments in the knee. *Osteoarthritis Cartilage*. 2006;14(11):1119-1125.

   doi: 10.1016/j.joca.2006.05.003

7. Brittberg M. Cell carriers as the next generation of cell therapy for cartilage repair: a review of the matrix-induced autologous chondrocyte implantation procedure. *Am J Sports Med*. 2010;38(6):1259-1271.

   doi: 10.1177/0363546509346395

8. Carr AJ, Robertsson O, Graves S, *et al*. Knee replacement. *Lancet*. 2012;379(9823):1331-1340.

   doi: 10.1016/S0140-6736(11)60752-6

9. Griffin DR, Weaver WM, Scumpia PO, Di Carlo D, Segura T. Accelerated wound healing by injectable microporous gel scaffolds assembled from annealed building blocks. *Nat Mater*. 2015;14(7):737-744.

   doi: 10.1038/nmat4294

10. Makris EA, Gomoll AH, Malizos KN, Hu JC, Athanasiou KA. Repair and tissue engineering techniques for articular cartilage. *Nat Rev Rheumatol*. 2015;11(1):21-34.

    doi: 10.1038/nrrheum.2014.157

11. Nordberg RC, Bielajew BJ, Takahashi T, Dai S, Hu JC, Athanasiou KA. Recent advancements in cartilage tissue engineering innovation and translation. *Nat Rev Rheumatol*. 2024;20(6):323-346.

    doi: 10.1038/s41584-024-01118-4

12. Cao Y, Liu C, Ye W, Zhao T, Fu F. Functional hydrogel interfaces for cartilage and bone regeneration. *Adv Healthc Mater*. 2025;14(6):e2403079.

    doi: 10.1002/adhm.202403079

13. Schuurman W, Levett PA, Pot MW, *et al*. Gelatin-methacrylamide hydrogels as potential biomaterials for fabrication of tissue-engineered cartilage constructs. *Macromol Biosci*. 2013;13(5):551-561.

    doi: 10.1002/mabi.201200471

14. Sun Z, Liu Q, Wang Z, *et al*. Hierarchical chitosan/polyvinyl alcohol/polyethylene glycol/nonwoven fabric micro/nanofiber composite membrane: a potential biomaterial for wound dressing. *Macromol Res*. 2023;31(12):1209-1215.

    doi: 10.1007/s13233-023-00204-y

15. Yang R, Sun J, Peng G, *et al*. Synergistic promotion of diabetic wound healing by glucose-responsive functional chitosan-based composite nanohydrogels. *Carbohydr Polym*. 2026;377:124835.

    doi: 10.1016/j.carbpol.2025.124835

16. Chen K, Wang J, Liu Q, *et al*. Sodium hyaluronate based multifunctional hydrogels delivering siRNA for sustained silencing of SMAD3: a novel strategy to treat intrauterine adhesions. *Carbohydr Polym*. 2026;380:125123.

    doi: 10.1016/j.carbpol.2026.125123

17. Zhou L, Chen S, Yang B, *et al*. 3D printing of cell-free implants: a promising avenue for cartilage regeneration and joint preservation. *Interdiscip Med*. 2026;4(5):e70161.

doi: 10.1002/inmd.70161

18. Moya A, Paquet J, Deschepper M, *et al*. Human mesenchymal stem cell failure to adapt to glucose shortage and rapidly use intracellular energy reserves through glycolysis explains poor cell survival after implantation. *Stem Cells*. 2018;36(3):363-376.

doi: 10.1002/stem.2763

19. Wang Q, Zhu W, Wang R, Weng X. Hierarchical 3D-printed scaffolds for osteochondral regeneration: from biomimetic design to functional integration. *Int J Bioprint*. 2025;11(4):4.

doi: 10.36922/ijb025120100

20. Yang M, Tang X, Tian Y, Liao Y, Zhu L, Chen H. Three-dimensional printing-based solutions for osteochondral regeneration: tailoring strategies to region-specific requirements. *Int J Bioprint*. 2026;12(2):025490507.

doi: 10.36922/ijb025490507

21. Li Z, Cao H, Xu Y, *et al*. Bioinspired polysaccharide hybrid hydrogel promoted recruitment and chondrogenic differentiation of bone marrow mesenchymal stem cells. *Carbohydr Polym*. 2021;267:118224.

doi: 10.1016/j.carbpol.2021.118224

22. van den Borne MPJ, Raijmakers NJH, Vanlauwe J, *et al*. International Cartilage Repair Society (ICRS) and Oswestry macroscopic cartilage evaluation scores validated for use in autologous chondrocyte implantation (ACI) and microfracture. *Osteoarthritis Cartilage*. 2007;15(12):1397-1402.

doi: 10.1016/j.joca.2007.05.005

23. Nguyen-Thanh T, Nguyen-Tran BS, Cruciani S, Dang-Cong T, Maioli M. A rabbit femoral trochlear defect model for chondral and osteochondral regeneration. *Acta Vet Brno*. 2022;91(3):293-301.

doi: 10.2754/avb202291030293

24. van der Sluijs JA, Geesink RGT, van der Linden AJ, Bulstra SK, Kuyer R, Drukker J. The reliability of the Mankin score for osteoarthritis. *J Orthop Res*. 1992;10(1):58-61.

doi: 10.1002/jor.1100100107

25. Laverty S, Girard CA, Williams JM, Hunziker EB, Pritzker KPH. The OARSI histopathology initiative—recommendations for histological assessments of osteoarthritis in the rabbit. *Osteoarthritis Cartilage*. 2010;18(suppl 3):S53-S65.

doi: 10.1016/j.joca.2010.05.029

26. Dorozhkin SV. Nanosized and nanocrystalline calcium orthophosphates. *Acta Biomater*. 2010;6(3):715-734.

doi: 10.1016/j.actbio.2009.10.031

27. Gan D, Jiang Y, Hu Y, *et al*. Mussel-inspired extracellular matrix-mimicking hydrogel scaffold with high cell affinity and immunomodulation ability for growth factor-free cartilage regeneration. *J Orthop Translat*. 2022;33:120-131.

doi: 10.1016/j.jot.2022.02.006

28. Hasturk O, Jordan KE, Choi J, Kaplan DL. Enzymatically crosslinked silk and silk-gelatin hydrogels with tunable gelation kinetics, mechanical properties and bioactivity for cell culture and encapsulation. *Biomaterials*. 2020;232:119720.

doi: 10.1016/j.biomaterials.2019.119720

29. Luo Y, Wang AT, Zhang QF, Liu RM, Xiao JH. RASL11B gene enhances hyaluronic acid-mediated chondrogenic differentiation in human amniotic mesenchymal stem cells via the activation of Sox9/ERK/Smad signals. *Exp Biol Med (Maywood)*. 2020;245(18):1708-1721.

doi: 10.1177/1535370220944375

30. Gittens RA, Scheideler L, Rupp F, *et al*. A review on the wettability of dental implant surfaces II: biological and clinical aspects. *Acta Biomater*. 2014;10(7):2907-2918.

doi: 10.1016/j.actbio.2014.03.032

31. Peterson L, Brittberg M, Kiviranta I, Åkerlund EL, Lindahl A. Autologous chondrocyte transplantation. *Am J Sports Med*. 2002;30(1):2-12.

doi: 10.1177/03635465020300011601

32. Temenoff JS, Mikos AG. Review: tissue engineering for regeneration of articular cartilage. *Biomaterials*. 2000;21(5):431-440.

doi: 10.1016/S0142-9612(99)00213-6

33. Gudas R, Gudaite A, Pocius A, *et al*. Ten-year follow-up of a prospective, randomized clinical study of mosaic osteochondral autologous transplantation versus microfracture for the treatment of osteochondral defects in the knee joint of athletes. *Am J Sports Med*. 2012;40(11):2499-2508.

doi: 10.1177/0363546512458763

34. Ye X, Gu W, Liu H, *et al*. Mild photothermal stimulation driven nanoparticles hybrid dual-network hydrogels for bone repair. *Small*. 2026;22(14):e12528.

doi: 10.1002/smll.202512528

35. Engler AJ, Sen S, Sweeney HL, Discher DE. Matrix elasticity directs stem cell lineage specification. *Cell*. 2006;126(4):677-689.

doi: 10.1016/j.cell.2006.06.044

36. Schuh E, Kramer J, Rohwedel J, *et al*. Effect of matrix elasticity on the maintenance of the chondrogenic phenotype. *Tissue Eng Part A*. 2010;16(4):1281-1290.

doi: 10.1089/ten.tea.2009.0614

37. Gomoll AH, Madry H, Knutsen G, *et al*. The subchondral bone in articular cartilage repair: current problems in the surgical management. *Knee Surg Sports Traumatol Arthrosc*. 2010;18(4):434-447.

doi: 10.1007/s00167-010-1072-x

38. Rivoallan N, Mueller M, Baudequin T, *et al*. Comparison of hydroxyapatite and honeycomb micro-structure in bone tissue engineering using electrospun beads-on-string fibers. *Int J Artif Organs*. 2024;47(8):642-649.

doi: 10.1177/03913988241268033

39. Yu K, Gao Q, Mi Y, *et al*. Computational investigation of a 3D-printed osteochondral interface scaffold with comprehensive interfacial mechanical properties. *Int J Bioprint*. 2025;11(2):353.

doi: 10.36922/ijb.8577

40. Yang Z, Wang B, Liu W, *et al*. In situ self-assembled organoid for osteochondral tissue regeneration with dual functional units. *Bioact Mater*. 2023;27:200-215.

doi: 10.1016/j.bioactmat.2023.04.002

41. Zhao X, Liu X, Huang Z, Ding K, Zhao Y, Bi Z. Construction of a 3D-printed polycaprolactone scaffold functionalized with extracellular matrix and an MSC-affinity peptide for articular cartilage repair. *Int J Bioprint*. 2026;12(4):026250258.

doi: 10.36922/ijb026250258

42. Zhou H, Lee J. Nanoscale hydroxyapatite particles for bone tissue engineering. *Acta Biomater*. 2011;7(7):2769-2781.

doi: 10.1016/j.actbio.2011.03.019

43. Mao B, Tian M, Yin Y, *et al*. A novel injectable cell-loaded hydrogel system for cartilage repair: in vivo and in vitro study. *Tissue Eng Part A*. Published online May 9, 2025.

doi: 10.1089/ten.tea.2025.0024

Appendix

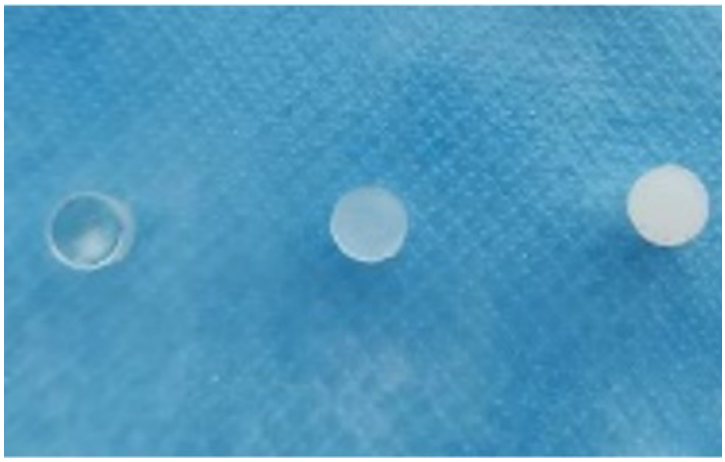


Figure A1. Samples for physicochemical characterization. From left to right: GelMA, GelMA/DHA, and GelMA/nHAp. Abbreviations: DHA: Dopamine-modified hyaluronic acid; GelMA: Gelatin methacryloyl; nHAp: Nano-hydroxyapatite.

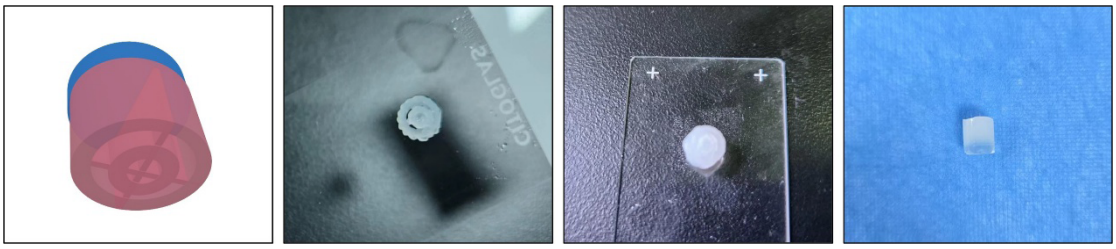


Figure A2. Scaffold architecture used for the animal experiments. From left to right: schematic illustration, cross-sectional view of the subchondral bone layer, top view of the cartilage layer, and side view of the bilayer scaffold.